UC Irvine
UC Irvine Previously Published Works

Title

Two-dimensional x-ray correlation spectroscopy of remote core states.

Permalink

https://escholarship.org/uc/item/12f538fx

Journal

Structural dynamics (Melville, N.Y.), 1(1)

ISSN

2329-7778

Authors

Healion, Daniel
Zhang, Yu
Biggs, Jason D
et al.

Publication Date

2014

DOI

10.1063/1.4833560

Peer reviewed

Two-dimensional x-ray correlation spectroscopy of remote core states

Daniel Healion, Yu Zhang, Jason D. Biggs, Weijie Hua, and Shaul Mukamel[a]

Department of Chemistry, University of California, 450 Rowland Hall, Irvine, California 92697-2025, USA

Nonlinear all-X-ray signals that involve large core-atom separation compared to the X-ray wavelengths may not be described by the dipole approximation since they contain additional phase factors. Expressions for the rotationally averaged 2D X-ray photon echo signals from randomly oriented systems that take this position-dependent phase into account for arbitrary ratio between the core separation and the resonant wavelength are presented. Application is made to the Se K-edge of a selenium dipeptide system. © *2013 Author(s). All article content, except where otherwise noted, is licensed under a Creative Commons Attribution 3.0 Unported License.* [http://dx.doi.org/10.1063/1.4833560]

I. INTRODUCTION

Nonlinear spectroscopy has been widely applied to excitonic systems spanning the vibrational[1,2] and electronic[3–5] response of chromophores in biological[6,7] and engineered[8] systems. X-ray free electron laser[9] sources strong enough to enable nonlinear processes[10,11] promise to extend these studies to core-excitons in molecules. These short, high-frequency pulses can probe the molecule on the time-scale of the attosecond period of the core-excitation and on the length-scale of the spatial extent of the resonant core orbital. Coherent excitations, which extend over long ranges (compared to the resonant wavelength), lead to violations of the dipole approximation. Quadripole core transitions on a single core are small, because the spatial extent of the core orbital is small compared to the exciting wavelength. Non-dipole transitions between cores can be modeled as dipole transitions multiplied by a complex phase factor dependent on the core location. While rare for IR and UV/Vis active chromophores, this kind of violation is expected to be the norm for strongly coupled, hard X-ray atomic core excitations in molecules. Time-resolved two- and three-pulse X-ray Raman experiments[12–15] avoid this difficulty by having the field interact twice with each chromophore, negating any dependence on the phase which is associated with the projection of the resonant core along the applied pulse wave vector.

The nonlinear response of quantum molecules to a classical external field can be expressed as a combination of multipoint correlation functions of the matter-field coupling term in the molecular Hamiltonian.[16] These multipoint functions in time and space, depend on both the spatial and temporal phase profiles of the applied field,

$$E(\mathbf{R}, t) = \varepsilon(t)\exp(i\mathbf{k} \cdot \mathbf{R} - i\omega_j t) + \text{c.c.} \tag{1}$$

For typical electronic and vibrational molecular transitions, the applied field wavelength is much longer than any exciton coherence length. In the dipole approximation, the signal is written as the sum of contributions from a dilute collection of molecules. The bulk polarization generated has a spatial dependence on the centers of the molecules, but the spatial phase of the field assumed to be nearly constant for transitions within the molecule ($\mathbf{k} \cdot \mathbf{R} \simeq 0$). In the optical regime, this phase is important only for chiral signals. For this reason, we will call the part of the signal which is included in the dipole approximation "nonchiral," and the remainder of

---

[a] smukamel@uci.edu

the signal the "chiral" part is generally more relevant for X-rays. The lowest terms in the correction for this approximation can be included by a Taylor expansion,

$$e^{i\mathbf{k}\cdot\mathbf{R}} \simeq 1 + i\mathbf{k}\cdot\mathbf{R} + (i\mathbf{k}\cdot\mathbf{R})^2 + \cdots. \tag{2}$$

This expansion should be avoided when system coherences exist on scales comparable to or larger than the exciting wavelength.

It is also necessary to average the response over the random orientations of the molecules relative to the laboratory frame defined by the wave vectors and polarizations of the applied pulses. Tensor techniques[17] are commonly used to analytically solve for the rotationally-averaged signals for $\mathbf{k}\cdot\mathbf{R} = 0$ when the matter-field coupling $(\hat{\mathcal{H}}_{\text{int}}(t))$ has no spatial phase dependence (i.e., $\hat{\mathcal{H}}_{\text{int}}(t) \sim \boldsymbol{\mu}_j \cdot \mathbf{e}_j$).[18] In the dipole approximation, a third order four-wave mixing signal will be proportional to the isotropic tensor product $I \sim \langle l_{a\alpha}l_{b\beta}l_{c\gamma}l_{d\delta}\rangle$, where $l_{a\alpha}$ are the Euler angles between the molecular (a,b,c,d) and laboratory $(\alpha, \beta, \gamma, \delta)$ frames of Ref. [17], and $\langle\cdots\rangle$ denotes the ensemble average over all possible rotation matrices $\hat{l}$. A core excitonic system including spatial phases with stationary holes will have a signal proportional to the phase rotationally averaged tensor: $I^{ph} \sim \langle l_{a\alpha}l_{b\beta}l_{c\gamma}l_{d\delta}e^{i\mathbf{k}_{ij}\cdot\mathbf{R}_{NM}}\rangle$, where $\mathbf{k}_{ij} = \mathbf{k}_i - \mathbf{k}_j$ is the wave vector difference between pulses i and j, and $\mathbf{R}_{NM}$ is the position vector difference between cores N and M. An analytic form of the averaged tensor was derived in Ref. [19]. This Phased Rotational Averaging (PRA) signal was applied to describe two-photon absorption in excitonic systems. Unlike the signal in the dipole approximation, this expression contains an explicit dependence on the wave vectors of the applied pulses, and the vectors connecting the chromophore positions, relative to the transition dipoles on the chromophores.

In this paper, we apply this averaging to a nonlinear hard X-ray technique. We show that different Liouville space pathways of this phase-dependent signal depend on different combinations of the applied pulse wave-vectors. This extra experimental knob allows groups of pathways to be isolated and measured separately. We consider experiments that are analogs of optical spectroscopy in molecular aggregates, with the molecular chromophores replaced by atomic core orbitals resonant with the X-ray frequencies of the applied fields. They contain terms with transitions resonant with separate cores on a molecule, and phases that depend on the distance between these cores. In nonlinear X-ray spectra, the relevant phases are determined by two length scales: the spatial extent of the core orbital and the distances between resonant cores. If the spatial extent of the core-orbital is small compared to the X-ray wavelength, the system obeys the local dipole approximation. If the spatial phase of the electric field is constant over a volume containing the molecule, the system obeys the global dipole approximation. X-ray pulses are short enough to probe valence electronic motions on subfemtosecond timescales with element-specific selectivity. In many interesting systems, e.g., large conjugated polyenes or transition metal compounds, only the local dipole approximation holds. In this study, we retain a simple single-electron Hamiltonian picture to describe the X-ray response for systems which obey the local but not the global dipole approximation. We introduce the dimensionless parameter $\kappa = R/\lambda$, where R is the distance between different cores and λ is a characteristic hard X-ray wavelength. In the global dipole approximation ($\kappa \ll 1$), rotational averaging leads to a contraction over tensor components of the response, the applied polarizations, and an isotropic tensor.[17] This has been widely applied to calculate the nonlinear response of systems of vibrational[18] and electronic[4] excitations.

Rotational averaging over a large collection of transition dipoles including a phase factor representing the position of each core is computationally laborious. Andrews *et al.* first derived expressions for the fourth order isotropic tensor[17] used for calculating the four-wave mixing signal. They subsequently considered a "phased" rotational averaging tensor, including an exponential containing a dot product between vectors in the molecular and laboratory frames.[19] Expressions for the four-wave mixing nonlinear response in the X-ray regime where $\kappa > 1$ are derived using this tensor. The photon-echo $\mathbf{k}_s = -\mathbf{k}_1 + \mathbf{k}_2 + \mathbf{k}_3$ signal contains pulse wave vector direction-dependent terms specific to each Liouville space path. In the $\kappa > 1$ regime, the nonlinear response is sensitive not only to the linear combination $\mathbf{k}_s$ of the incident pulse wave-vectors, but to their individual, component directions as well. The dependence of the photon echo signal in photosynthetic exciton systems on the applied field wave vectors and the polarizations of the applied pulses has been investigated by Mercer *et al.*[20,21] We adopt the same

typical boxcar geometry. We apply these results to a model system of a selenium dipeptide, with $R = 5.803$ Å and $\lambda = 0.979$ Å, making $\kappa = 5.924$. The signal is shown to contain a factor dependent on both the polarizations and the directions of the wave vectors of the applied pulses. Numerical results are then presented.

II. THE PHOTON ECHO SIGNAL FOR ARBITRARY κ

First, we discuss the general case by including a spatial phase in the photon echo signal for an aggregate of coupled two-level systems, showing an analytic solution exists for the collinear experiment, in which the applied pulses have the same wave vector. Then, we present the X-ray experiment for noncollinear pulses. Expressions for the X-ray photon echo signal were derived in Ref. 22. We consider an electronic Hamiltonian

$$\hat{\mathcal{H}} = \hat{\mathcal{H}}_o + \hat{\mathcal{H}}_{\text{int}}(t) \tag{3}$$

partitioned between a material part

$$\hat{\mathcal{H}}_o = \sum_r \epsilon_r c_r^\dagger c_r + \sum_{rstu} V_{rs,tu} c_r^\dagger c_s^\dagger c_t c_u \tag{4}$$

defined in terms of the orbital creation $c_i^\dagger$ and annihilation c_i operators, with orbital energies ϵ_r, coupled by the Coulomb interaction

$$V_{rs,tu} = \int \frac{\phi_r^*(\mathbf{r})\phi_s^*(\mathbf{r}')\phi_t(\mathbf{r}')\phi_s(\mathbf{r})}{|\mathbf{r} - \mathbf{r}'|} \mathrm{d}\,\mathbf{r}\,\mathrm{d}\,\mathbf{r}'. \tag{5}$$

The nuclei are considered fixed in this treatment. The explicit time-dependence of the Hamiltonian in Eq. (3) is through an externally applied classical field

$$\hat{\mathcal{H}}_{\text{int}}(t) = -\int \boldsymbol{\mu}(\mathbf{r}, t) \cdot \mathbf{E}(\mathbf{r}, t)\mathrm{d}\,\mathbf{r}. \tag{6}$$

The nonlinear response formalism[5] casts the signal as the heterodyne-detected overlap between the field emitted by the material polarization generated by the first three pulses overlapped with a fourth pulse. The electric field is written

$$E(\mathbf{r}, t) = \sum_{j=1}^4 \mathbf{e}_j \varepsilon_j(t - \tau_j)\exp[+i\mathbf{k}_j \cdot \mathbf{r} - i\omega_j(t - \tau_j)] + \text{c.c.}, \tag{7}$$

with polarization vectors $\mathbf{e}_j$, envelopes ε_j, arrival times τ_j, and central frequencies ω_j. In the frequency domain, this expression becomes

$$\varepsilon_j(\omega) = \int_{-\infty}^{\infty} e^{i(\omega - \omega_j)t}\varepsilon_j(t)\,\mathrm{d}\,\omega. \tag{8}$$

The dipole operator coupling the core-orbital to the field

$$\boldsymbol{\mu}(\mathbf{r}) = \sum_N \hat{\boldsymbol{\mu}}\,\delta(\mathbf{r} - \mathbf{R}_N) \tag{9}$$

also contains a spatial dependence on the location of the chromophore $\mathbf{R}_N$, which is a two level subunit in the aggregate, or a resonant core in the X-ray experiment. The dipole operator in the orbital basis is defined as

$$\hat{\boldsymbol{\mu}} = \sum_{aN} \boldsymbol{\mu}_{aN} c_a^\dagger c_N + \text{c.c.}, \tag{10}$$

where

$$\boldsymbol{\mu}_{aN} = \int \phi_a^*(\mathbf{r})\mathbf{r}\phi_N(\mathbf{r})\mathrm{d}\,\mathbf{r}. \tag{11}$$

The eigenstates of $\hat{\mathcal{H}}_o$ are the ground and valence excited states $|g\rangle, |g'\rangle, \ldots$, are singly core-excited states with holes on the N or M core, respectively, $|e_N\rangle, |e_M\rangle, \ldots$, and the doubly core excited states $|f_{NM}\rangle$ (see Fig. 1). We make the local dipole approximation described in the introduction by assuming the matrix elements of the dipole operator

$$\mu_{e_N g}^{m_j} = \langle e_N | \hat{\mu}_{m_j} | g \rangle = e^{i\mathbf{k}_j \cdot \mathbf{R}_N} \langle e_N | (r_{m_j} - R_{Nm_j}) | g \rangle \tag{12}$$

are taken relative to the position of the chromophore, with the phase of the jth electric pulse at that chromophore.

The general expression for the PRA signal, after accounting for a spatial phase, and an arbitrary rotation of the molecular system by an Euler rotation matrix $\hat{l}$, modifies each dipole, $\mu^{m_j} \rightarrow \mu^{m_j} l_{m_i f_i} \exp[ik_j \cdot R_j]$, leading to the following tensor average:

$$\langle l_{m_1 f_1} l_{m_2 f_2} l_{m_3 f_3} l_{m_4 f_4} \exp[i(-\mathbf{k}_1 \cdot \mathbf{R}_N + \mathbf{k}_2 \cdot \mathbf{R}_{N'} + \mathbf{k}_3 \cdot \mathbf{R}_M - \mathbf{k}_s \cdot \mathbf{R}_{M'})]\rangle. \tag{13}$$

In the photon echo experiment, $\mathbf{k}_s = -\mathbf{k}_1 + \mathbf{k}_2 + \mathbf{k}_3$. Substituting this into Eq. (13), we get

$$\langle l_{m_1 f_1} l_{m_2 f_2} l_{m_3 f_3} l_{m_4 f_4} \exp[i(-\mathbf{k}_1 \cdot (\mathbf{R}_N - \mathbf{R}_{M'}) + \mathbf{k}_2 \cdot (\mathbf{R}_{N'} - \mathbf{R}_{M'}) + \mathbf{k}_3 \cdot (\mathbf{R}_M - \mathbf{R}_{M'})])]\rangle. \tag{14}$$

The indices $m_{1...4}$ ($f_{1...4}$) refer to tensors defined in the molecular (laboratory) frame of reference. $l_{m_i f_i}$ are matrix elements of the Euler rotation matrix, and $\langle \cdots \rangle \equiv \int \cdots \mathrm{d}\,\hat{l}$ is the ensemble average over the relative orientations of these two frames. If Eq. (14) can be placed into a form with a single dot product in the exponential, the formalism given in Ref. 19 can be applied. Two different ways are now presented to perform this simplification.

III. PHOTON ECHOES IN A COLLINEAR PULSE CONFIGURATION

The collinear pulse geometry is the simplest; we now apply the non-dipole averaging to a collinear photon-echo signal on a model aggregate of coupled two-level systems (see Fig. 2).[4] Phase-cycling is a technique used to extract an equivalent to the photon echo by varying the phases between pulses. Originally used in nuclear magnetic resonance (NMR),[23] it has been adapted to multidimensional optical experiments.[24–27] If $\mathbf{k}_{1,2,3,s} \equiv \mathbf{k}$, then the dot products in Eq. (14) can be combined.
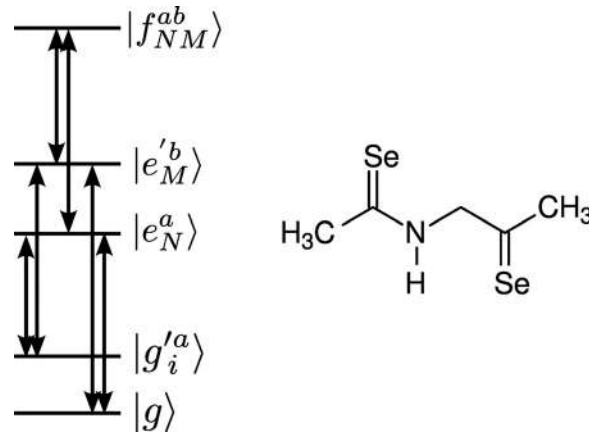

FIG. 1. Level diagram for the valence, single and double core-excited states of the selenium dipeptide. Double-arrows mark dipole coupled states. The wavelength (λ_{Se}) resonant with the Se K-edge transition (12658.00 eV) is 0.979 Å, and the Se atoms are separated by 5.803 Å (5.924 λ_{Se}).
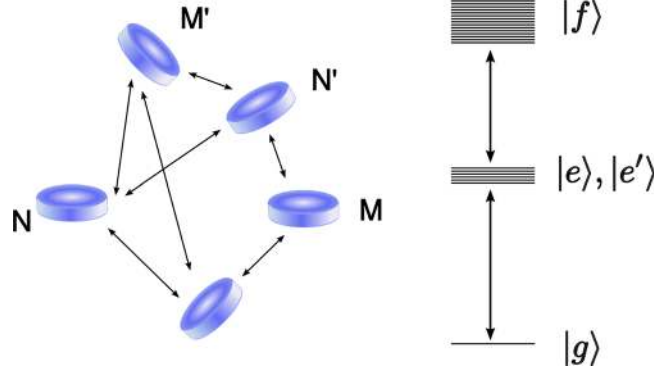
FIG. 2. System of coupled two-level systems.

We define the excitonic dipole operator

$$\hat{\boldsymbol{\mu}} = \sum_n \boldsymbol{\mu}_n B_n^\dagger + \boldsymbol{\mu}_n^\dagger B_n \tag{15}$$

and the single

$$|e\rangle = \sum_N C_{eN} B_N^\dagger |g_o\rangle \tag{16}$$

and doubly

$$|f\rangle = \sum_{NM} C_{f,NM} B_N^\dagger B_M^\dagger |g_o\rangle \tag{17}$$

excited states in terms of local chromophore excitation creation $(B_N^\dagger)$ and annihilation (B_N) operators. The eigenstate dipole operators are expanded in the local state basis using this notation. The response contains spatial phase factors that depend on the chromophore positions (see Fig. 3), and an additional sum over local sites $N, N', M,$ and M'. The signal is a sum of three terms

$$S_{\text{tot}}(\Omega_1, t_2, \Omega_3) = S_{\text{GSB}}(\Omega_1, t_2, \Omega_3) + S_{\text{ESE}}(\Omega_1, t_2, \Omega_3) + S_{\text{ESA}}(\Omega_1, t_2, \Omega_3). \tag{18}$$

The ground state bleaching,

$$\begin{aligned}
S_{\text{GSB}}(\Omega_3, t_2, \Omega_1) = \sum_{e,e'} \sum_{NN'MM'} \left(\frac{-i}{\hbar}\right)^3 & \mu_N^{m_1} \mu_{N'}^{m_2} \mu_M^{m_3} \mu_{M'}^{m_4} e_1^{f_1} e_2^{f_2} e_3^{f_3} e_4^{f_4} \\
& \times \langle l_{m_1 f_1} l_{m_2 f_2} l_{m_3 f_3} l_{m_4 f_4} \exp[i\mathbf{k}\cdot(\mathbf{R}_{NN'} + \mathbf{R}_{MM'})]\rangle \\
& \times C_{eN}^* C_{eN'} C_{e'M} C_{e'M'}^* \frac{|\varepsilon(\omega_{eg})|^2 |\varepsilon(\omega_{e'g})|^2}{(\Omega_1 - \omega_{ge} + i\gamma)(\Omega_3 - \omega_{e'g} + i\gamma)},
\end{aligned} \tag{19}$$

and stimulated emission term,

$$\begin{aligned}
S_{\text{ESE}}(\Omega_3, t_2, \Omega_1) = \sum_{e,e'} \sum_{nn'mm'} \left(\frac{-i}{\hbar}\right)^3 & \mu_N^{m_1} \mu_{N'}^{m_2} \mu_M^{m_3} \mu_{M'}^{m_4} e_1^{f_1} e_2^{f_2} e_3^{f_3} e_4^{f_4} \\
& \times \langle l_{m_1 f_1} l_{m_2 f_2} l_{m_3 f_3} l_{m_4 f_4} \exp[i\mathbf{k}\cdot(\mathbf{R}_{NN'} + \mathbf{R}_{MM'})]\rangle \\
& \times C_{eN}^* C_{e'N'} C_{eM} C_{e'M'}^* \frac{|\varepsilon(\omega_{eg})|^2 |\varepsilon(\omega_{e'g})|^2 e^{-i\omega_{e'e} t_2 - \gamma' t_2}}{(\Omega_1 - \omega_{ge} + i\gamma)(\Omega_3 - \omega_{e'g} + i\gamma)},
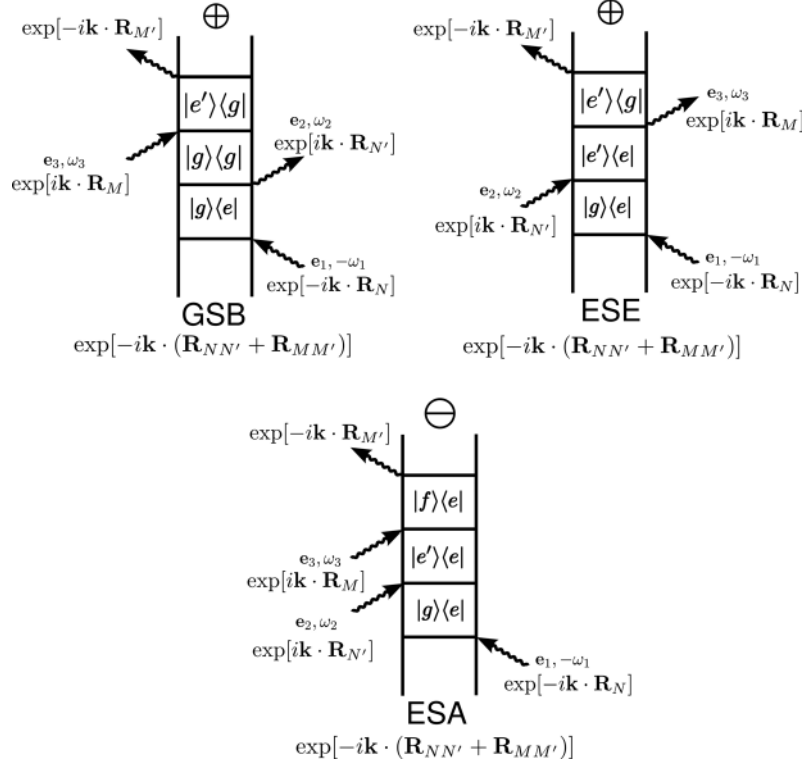\end{aligned} \tag{20}$$

FIG. 3. Ladder diagrams and phase factors contributing to the response for the coupled two-level systems, corresponding to Eqs. (19)–(21).

contain only singly excited states. The expression for the excited state absorption

$$
S_{\text{ESA}}(\Omega_3, t_2, \Omega_1) = \sum_{e,e'} \sum_{NN'MM'} \sum_{PQ} \left(\frac{-i}{\hbar}\right)^3 \mu_N^{m_1} \mu_{N'}^{m_2} \mu_M^{m_3} \mu_{M'}^{m_4} e_1^{f_1} e_2^{f_2} e_3^{f_3} e_4^{f_4}
$$
$$
\times \langle l_{m_1 f_1} l_{m_2 f_2} l_{m_3 f_3} l_{m_4 f_4} \exp[i\mathbf{k} \cdot (\mathbf{R}_{NN'} + \mathbf{R}_{MM'})] \rangle
$$
$$
\times C_{eN} C^*_{e'N'} (C^*_{f,MP} + C^*_{f,PM}) C_{e,P} C^*_{e',Q} (C_{f,M'Q} + C_{f,QM'})
$$
$$
\times \frac{\varepsilon^*(\omega_{ef}) \varepsilon(\omega_{fe'}) \varepsilon^*(\omega_{eg}) \varepsilon(\omega_{e'g}) e^{-i\omega_{e'e} t_2 - \gamma' t_2}}{(\Omega_1 - \omega_{ge} + i\gamma)(\Omega_3 - \omega_{fe} + i\gamma)}. \tag{21}
$$

The tensor averages $\langle l_{m_1 f_1} \ldots \rangle$ in these expressions can be evaluated using the results of Appendix B. Only homogeneous broadening was considered in the derivation of Eqs. (19)–(21).

The generic excitonic systems described above have delocalized eigenstates, and the four pulses can interact at four points in space (R_N, $R_{N'}$, R_M, $R_{M'}$ in Fig. 3). Core holes, in contrast, are localized and the applied pulses must create and destroy a hole on the same site. The signal thus only involves two cores ($R_{N,M}$). One of the two selenium atoms in Fig. 1 is closer to the peptide nitrogen than the other, resulting in a slightly different chemical environment. We assume the through-space coupling between the core holes is much smaller than their orbital energy splitting, leading to a nearly stationary core-hole. A thorough treatment of the core-hole hopping dynamics between equivalent cores in identical chemical environments has yet to be performed, and will be the focus of future studies. The core-excitations have the form of excitations from stationary cores to diffuse frontier orbitals, forcing each participating core to absorb and emit with the X-ray field, and making the $\mathbf{k} \cdot \mathbf{R}$ factors in Eqs. (19)–(21) vanish and the dipole approximation holds when the wavevectors of all four pulses are the same. The form of the X-ray excitations, with stationary core-holes is the reason the four-point diagrams in Fig. 3
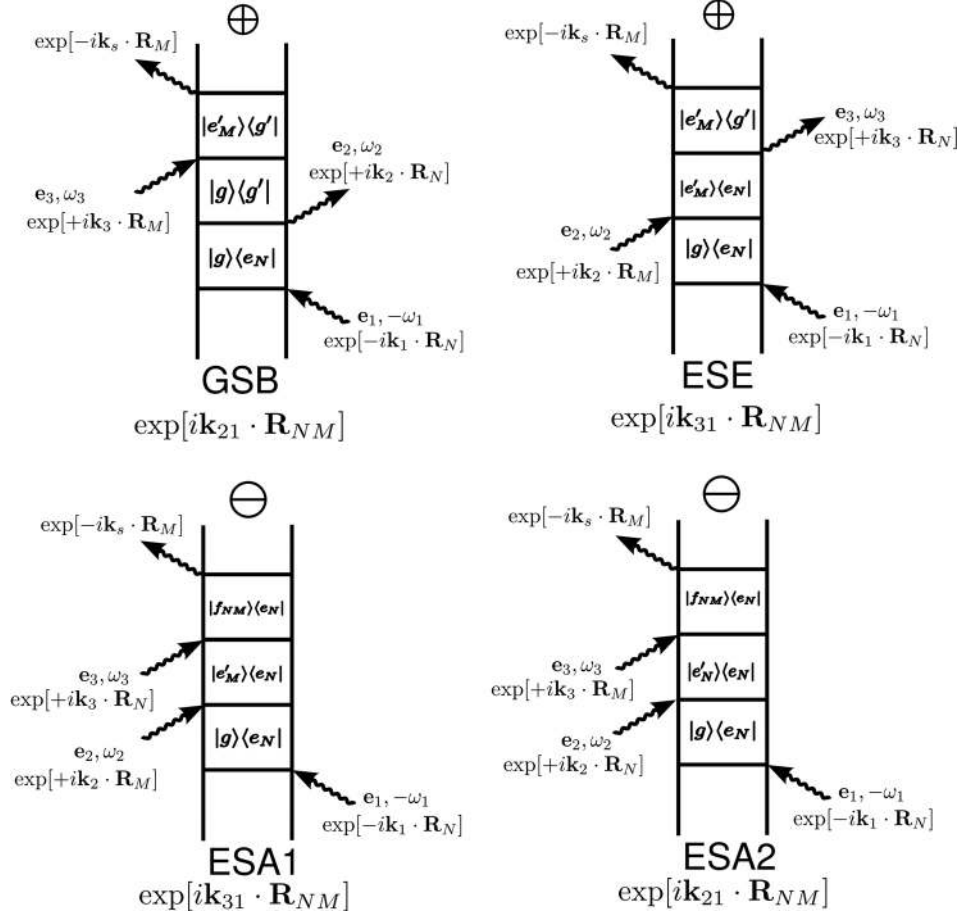
FIG. 4. Ladder diagrams for the photon echo signal, including the wave vector dependent phase, corresponding to Eqs. (23)–(26).

simplify to the two-point diagrams given in Fig. 4. For collinear pulses, the photon echo X-ray signal carries no dependence on the intercore separation, only when the applied pulses have different wavevectors will the signal contain a dependence on the intercore distance.

IV. X-RAY PHOTON ECHO FOR NONCOLLINEAR PULSES

We now describe the X-ray photon echo signal for noncollinear pulses. Ladder diagrams for the X-ray photon echo signal are given in Fig. 4. Unlike the coupled, two-level system case, each excitation $(e, e', \ldots)$ is associated with its own core, which we label with subscripts $(e_N, e'_M, \ldots)$. The total signal is the sum of four contributions

$$S_{\mathrm{PRA}}(\Omega_3, t_2, \Omega_1) = S_{\mathrm{GSB}}(\Omega_3, t_2, \Omega_1) + S_{\mathrm{ESE}}(\Omega_3, t_2, \Omega_1)$$
$$+ S_{\mathrm{ESA1}}(\Omega_3, t_2, \Omega_1) + S_{\mathrm{ESA2}}(\Omega_3, t_2, \Omega_1), \tag{22}$$

the ground state bleaching

$$S_{\mathrm{GSB}}(\Omega_3, t_2, \Omega_1) = \sum_{g', e_N, e'_M} \mu_{ge_N}^{m_1} \mu_{e_N g'}^{m_2} \mu_{e'_M g}^{m_3} \mu_{g' e'_M}^{m_4} \langle l_{m_1 f_1} l_{m_2 f_2} l_{m_3 f_3} l_{m_4 f_4} \exp[i\mathbf{k}_{21} \cdot \mathbf{R}_{NM}] \rangle$$
$$\times \frac{-16\pi^4 e^{-i\omega_{gg'} t_2 - \gamma t_2} \varepsilon_{f_1}^*(\omega_{ge_N}) \varepsilon_{f_2}(\omega_{e_N g'}) \varepsilon_{f_3}(\omega_{e'_M g}) \varepsilon_{f_4}^*(\omega_{g' e'_M})}{(\Omega_1 - \omega_{ge_N} + i\gamma)(\Omega_3 - \omega_{e'_M g'} + i\gamma)}, \tag{23}$$

the excited state emission

$$S_{\text{ESE}}(\Omega_3, t_2, \Omega_1) = \sum_{g', e_N, e_M'} \mu_{ge_N}^{m_1} \mu_{e_M'g}^{m_2} \mu_{e_Ng'}^{m_3} \mu_{g'e_M'}^{m_4} \langle l_{m_1f_1} l_{m_2f_2} l_{m_3f_3} l_{m_4f_4} \exp[i\mathbf{k}_{31} \cdot \mathbf{R}_{NM}]\rangle$$
$$\times \frac{-16\pi^4 e^{-i\omega_{e_M'e_N}t_2 - \gamma t_2} \varepsilon_{f_1}^*(\omega_{ge_N}) \varepsilon_{f_2}(\omega_{e_M'g}) \varepsilon_{f_3}(\omega_{e_Ng'}) \varepsilon_{f_4}^*(\omega_{g'e_M'})}{(\Omega_1 - \omega_{ge_N} + i\gamma)(\Omega_3 - \omega_{e_M'g'} + i\gamma)}, \tag{24}$$

and excited state absorption with two orderings of core-excitations

$$S_{\text{ESA1}}(\Omega_3, t_2, \Omega_1) = -\sum_{g', e_N, e_M'} \mu_{ge_N}^{m_1} \mu_{e_M'g}^{m_2} \mu_{f_{NM}e_M'}^{m_3} \mu_{e_Nf_{NM}}^{m_4} \langle l_{m_1f_1} l_{m_2f_2} l_{m_3f_3} l_{m_4f_4} \exp[i\mathbf{k}_{31} \cdot \mathbf{R}_{NM}]\rangle$$
$$\times \frac{-16\pi^4 e^{-i\omega_{e_M'e_N}t_2 - \gamma t_2} \varepsilon_{f_1}^*(\omega_{ge_N}) \varepsilon_{f_2}(\omega_{e_M'g}) \varepsilon_{f_3}(\omega_{f_{NM}e_M'}) \varepsilon_{f_4}^*(\omega_{e_Nf_{NM}})}{(\Omega_1 - \omega_{ge_N} + i\gamma)(\Omega_3 - \omega_{f_{NM}e_N} + i\gamma)}, \tag{25}$$

$$S_{\text{ESA2}}(\Omega_3, t_2, \Omega_1) = -\sum_{g', e_N, e_N'} \mu_{ge_N}^{m_1} \mu_{e_N'g}^{m_2} \mu_{f_{NM}e_N'}^{m_3} \mu_{e_nf_{NM}}^{m_4} \langle l_{m_1f_1} l_{m_2f_2} l_{m_3f_3} l_{m_4f_4} \exp[i\mathbf{k}_{21} \cdot \mathbf{R}_{NM}]\rangle$$
$$\times \frac{-16\pi^4 e^{-i\omega_{e_N'e_N}t_2 - \gamma t_2} \varepsilon_{f_1}^*(\omega_{ge_N}) \varepsilon_{f_2}(\omega_{e_N'g}) \varepsilon_{f_3}(\omega_{f_{NM}e_N'}) \varepsilon_{f_4}^*(\omega_{e_nf_{NM}})}{(\Omega_1 - \omega_{ge_N} + i\gamma)(\Omega_3 - \omega_{f_{NM}e_N} + i\gamma)}. \tag{26}$$

With heterodyne detection, it is possible to measure the real and imaginary parts of the generated field by interference with the last field. We assume we are measuring the real part of the signal. The lineshape functions

$$\int_{-\infty}^{+\infty} \theta(t) e^{i(\Omega - \omega_{rs})t - \gamma_+ t} \mathrm{d}t = \frac{i}{\Omega - \omega_{rs} + i\gamma_+}, \tag{27}$$

the frequency domain form of the electric pulses

$$\varepsilon_j(\omega) = [e^{-(\omega - \omega_j)^2/2\sigma_j^2} + e^{-(\omega + \omega_j)^2/2\sigma_j^2}]\frac{1}{2\sigma_j^2}, \tag{28}$$

and the perturbative factor $(-i/\hbar)^3$ contribute to the $-16\pi^4$ factor in each expression. A resonant contributions to the fourth-order signal only include terms where the number of core-excitons created equal the number destroyed. We neglect core-hole migration, so that only two cores contribute to each term. Equations (22)–(26) will now be applied to calculate the signal for a model selenium dipeptide.

V. APPLICATION TO SELENIUM DIPEPTIDE

Charge and energy transfer in protein systems is a field of growing technical interest as these systems are currently more efficient than artificially designed catalysts and solar cells. Selenium is isoelectronic with oxygen and has been used to tag proteins[28] and oligonucleotides[29] for determining their structure using the multiwavelength anomalous dispersion (MAD) technique. Recently, small oligotides were synthesized with selenium substitute directly for the oxygen on the amide backbone.[30] As this backbone is often implicated in charge transfer in proteins, a selenium dipeptide system (Fig. 1) is an attractive system to investigate these nonlinear X-ray effects. The core-excited states of the selenium dipeptide (see Fig. 1) are treated using the orbital approximation and neglecting core-relaxation. The X-ray absorption near edge structure (XANES) in this approximation is shown in Fig. 5, with the applied pulse power spectrum in blue. An active orbital space of the four virtual and four occupied orbitals are taken and used to approximate the core singly $(|e_N\rangle = c_a^\dagger c_N|g\rangle, \epsilon_{e_N} = \omega_{aN})$ and doubly $(|f_{NM}\rangle = c_a^\dagger c_b^\dagger c_M c_N|g\rangle, \epsilon_{f_{NM}} = \omega_{aN} + \omega_{bM})$ core excited states. The valence states are also treated using the orbital approximation $(|g'\rangle = c_a^\dagger c_i|g\rangle, \epsilon_{g'} = \omega_{ai})$. All orbitals, energies, and dipole matrix
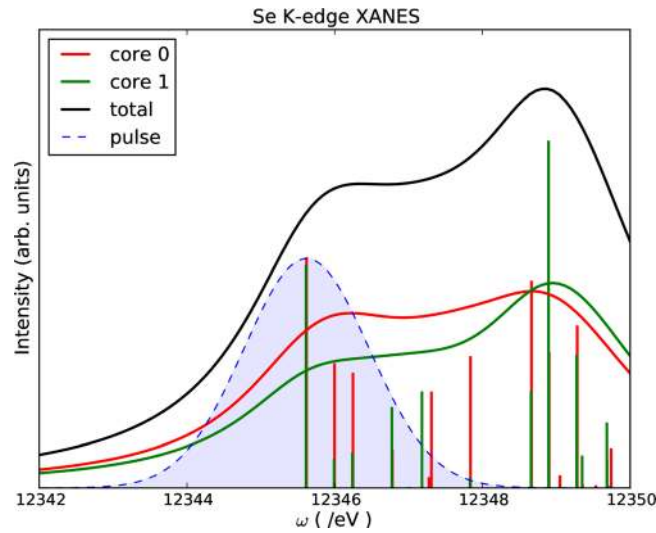
FIG. 5. Se K-edge XANES spectra of the selenium dipeptide system. Blue line is the power spectrum of the pulse used for the 2D signals.

elements were calculated using the GAUSSIAN 03 code,[31] using the B3LYP functional[32] and the aug-cc-pVTZ basis set.[33,34] Each peak is broadened by a Lorentzian with a 2.20 eV FWHM[35] representing the core-hole lifetime. The level of theory is crude, as demonstrated by the large energy shift between the calculated core-edge in Fig. 5, and the experimental 12.65 keV Se K-edge,[35] but is expected to qualitatively reproduce the XANES spectra.

We assume a boxcar pulse geometry (see Fig. 6), with an apex angle α of $30°$. This is larger than the small solid angle usually chosen for experimental convenience. The apex angle in the boxcar geometry (see Fig. 7) fixes the size of the wavevector differences that contribute to κ; by increasing the difference between the wave vectors, the non-dipole approximation contribution to the signal will be larger. We define "out" polarizations, which are included in a plane containing the center of the pyramid and the wave vector, and "about" polarizations, which are perpendicular to both the wave vector and the "out" polarization (see Fig. 7). Following Appendix B, the signal is a linear combination of nineteen components, weighted by the spherical Bessel function $(j_n(\kappa))$. We choose the all "out" polarization with a boxcar geometry with an apex angle of $30°$. The result is shown in Fig. 8. We find that the nonchiral part of the signal—the signal calculated using the dipole approximation—is roughly three orders of magnitude smaller than the chiral signal. This could be predicted from the geometry of the
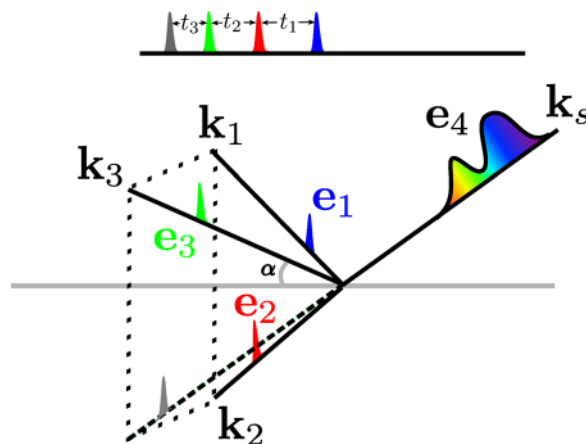

FIG. 6. Boxcar pulse geometry with apex angle α, field wave vectors $\mathbf{k}_{1-3,s}$ and polarizations $\mathbf{k}_{1-4}$.
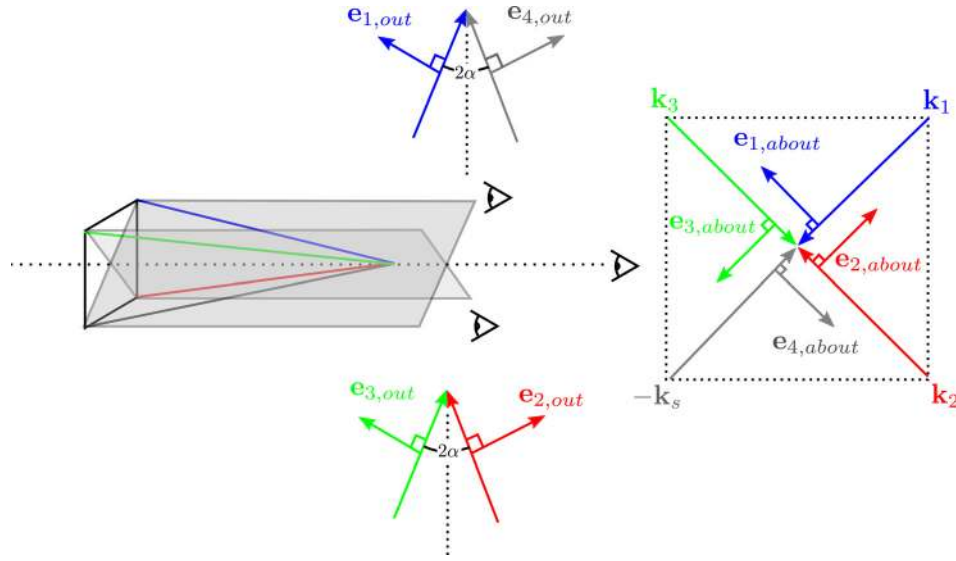
FIG. 7. Polarizations defined in boxcar geometry. $\mathbf{e}_j \perp \mathbf{k}_j \forall j$, $\mathbf{e}_{j,out}$ shares the plane containing the axis of the pyramid and $\mathbf{k}_j$; $\mathbf{e}_{j,about} = \mathbf{e}_{j,out} \times \mathbf{k}_j$.

selenium atoms, as shown by the vertical line in Fig. 9, the first order contribution to the response is expected to be weak.

The PRA signal can be written as a linear combination of components, which is written conveniently written in block matrix form, with five components $(V_{L1...L5})$ given in Appendix B. Each block is weighted by a spherical Bessel function $j_{1...5}(\kappa)$ with an argument $\kappa = R_{NM}/\lambda$. When the resonant core wavelength (λ) is much larger than the intercore distance (R_{NM}), only $j_0(\kappa)$ is nonzero, and only the first block corresponding to the dipole allowed transitions (V_{L0}) contributes to the signal. The signals are broken down into their contributions from each matrix element of the V_L vector in Figs. 10–14. Although these may not be measured separately, they provide a framework for interpreting the overall signal given in Fig. 8. The nonchiral signal in Fig. 8 is the sum of the three signals in Fig. 10, the nonchiral part is the sum of the remaining contributions in Figs. 11–14. The nonchiral signal is dominated by the last signal from Fig. 14, and we include the rest to show there is additional information in these signals. The first block of V_L in Fig. 10 represents the dipole-approximated signals and are fairly low in amplitude compared to the rest of the signals, as predicted above. The next block in Fig. 11 contains several contributions with a comparable intensity to the nonchiral signal, but with opposite and
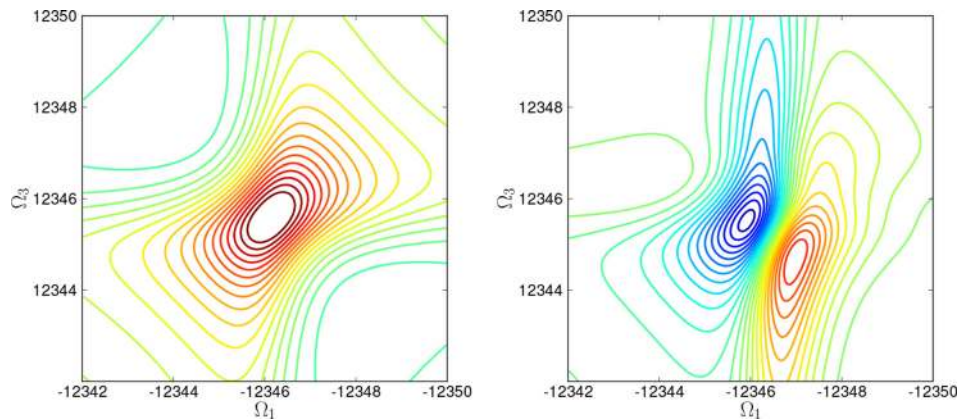

FIG. 8. (Left) Nonchiral (with 60 contours spanning $\pm 3 \times 10^{-4}$) and (right) chiral (60 contours spanning spanning ± 1) contributions to the real part of the PRA signal. Notice that the chiral signal is much stronger.
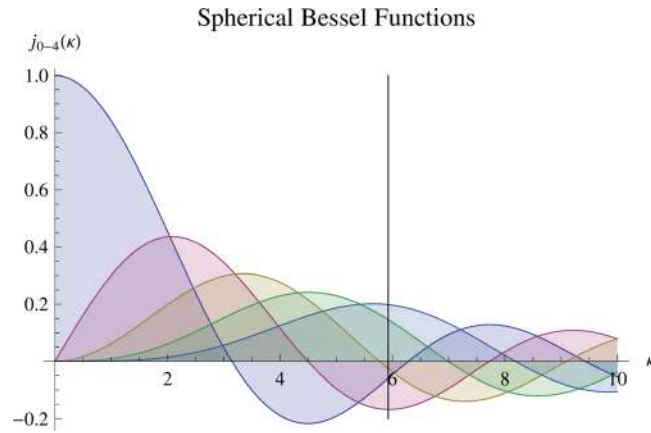
FIG. 9. Spherical Bessel functions $j_{0-4}(\kappa)$, with the inter-atom Selenium distance (in units of $\lambda = 1.021\text{Å}$) given by the vertical line.

canceling phases ((iv) and (v); (viii) and (ix)). The unique contributions (vi) and (vii) are much lower in amplitude, and contribute negligibly to the final signal. The third block contains several contributions with strong and noncanceling weights, taken together the signals (x)–(xiii) should contribute at ~1% of the total signal intensity, which can be compared to the signal
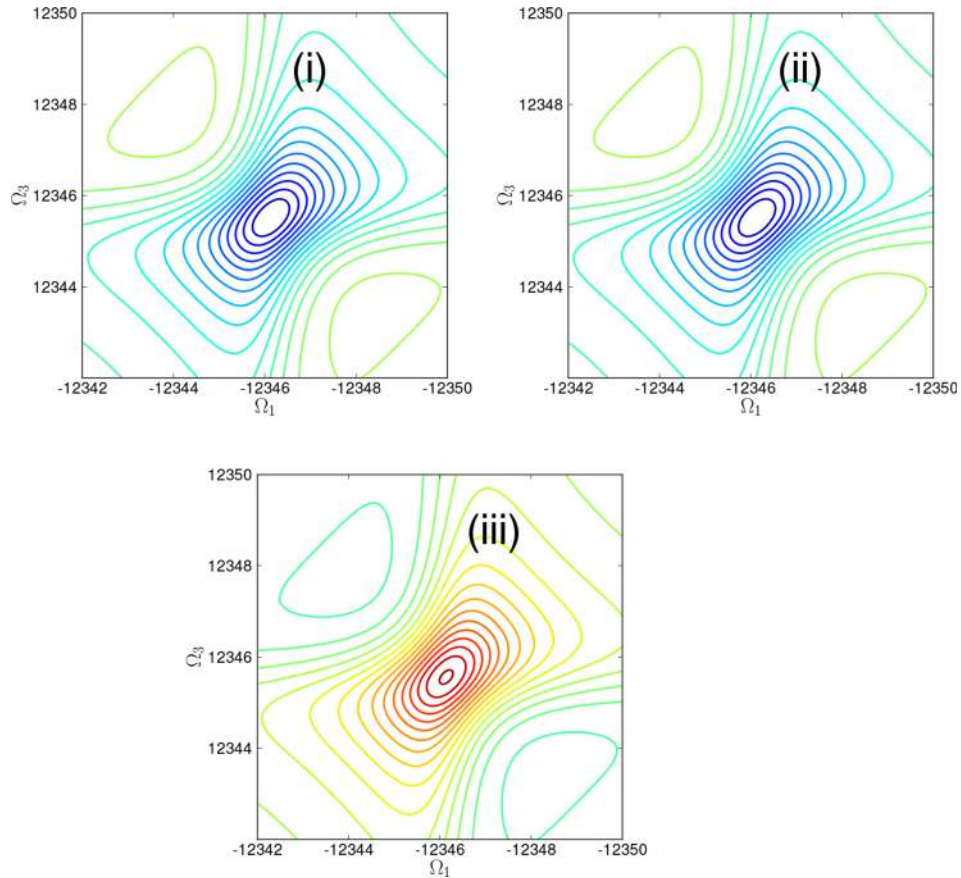

FIG. 10. Contributions from the chiral parts of the V_L vector [Eq. (B1)], the first three matrix elements. There are 30 contour lines (i), (ii) from $\pm 7 \times 10^{-5}$, and (iii) from $\pm 5 \times 10^{-4}$.
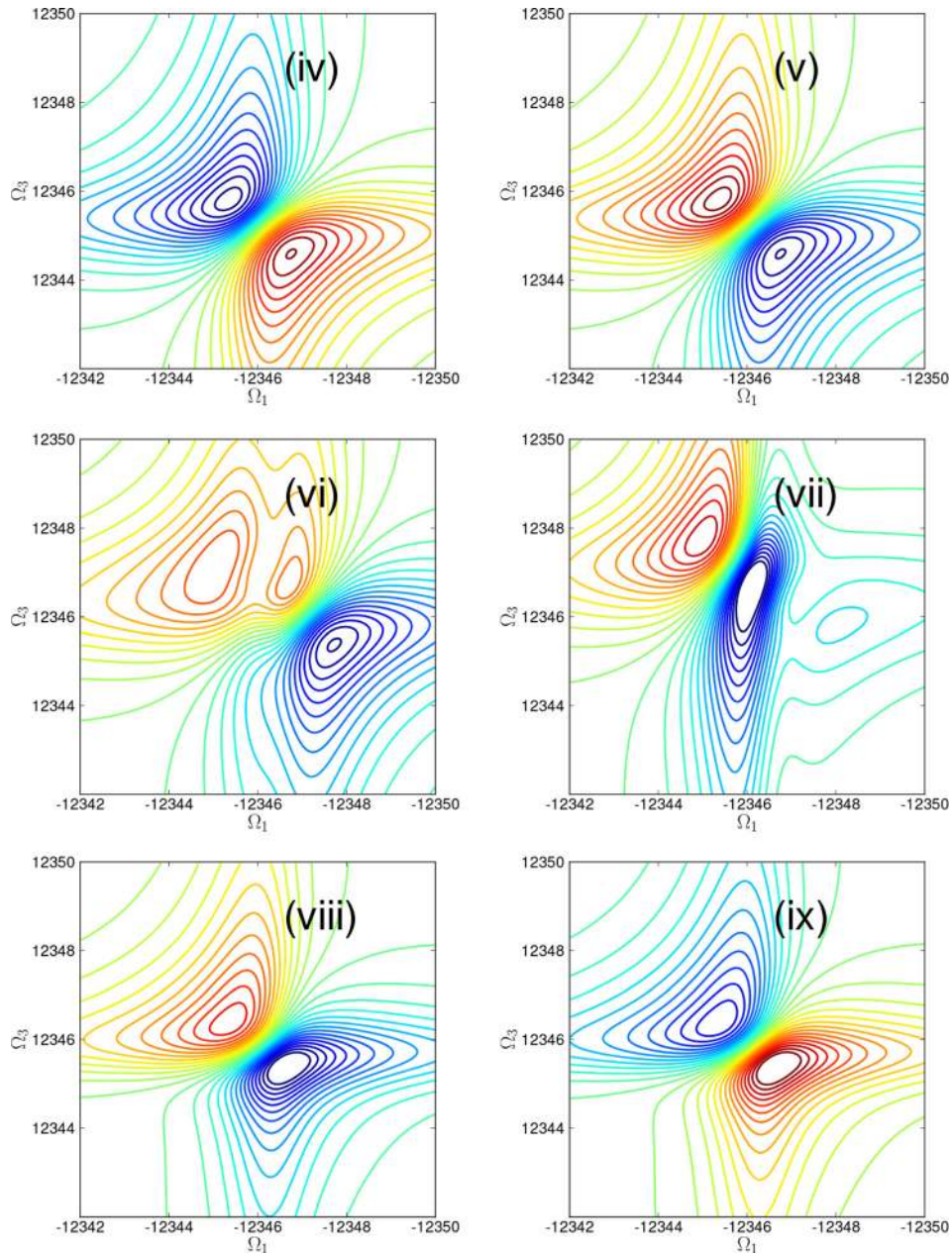
FIG. 11. Contributions from the second block, nonchiral parts of the V_L vector [Eq. (B1)], the contour ranges are $\pm 2 \times 10^{-4}$, $\pm 2 \times 10^{-4}$, $\pm 3 \times 10^{-7}$, $\pm 1 \times 10^{-7}$, $\pm 1.5 \times 10^{-5}$, $\pm 1.5 \times 10^{-5}$, respectively.

very intense (xvi) contribution. The most intense contribution to the signal is in the last matrix element, shown in Fig. 14.

We next turn to signals that can be experimentally discriminated, by varying the polarizations of the measurement. There are $2^4 = 16$ choices of polarizations for each choice of apex angle in the boxcar geometry. The different signals for $\theta = 30°$ are shown in Fig. 15. The signals form two groups with minor changes in the lineshapes and sign changes. Spectra in which the polarizations are paired (that have two "out" polarizations and two "about" polarizations, as described in Fig. 7) form one group, the other group has one polarization of one type, and the rest of the other. For an apex angle near zero, the chiral XXXY signal would be in the second group, and the nonchiral XXYY, XYXY, and XYYX signals would be in the first.
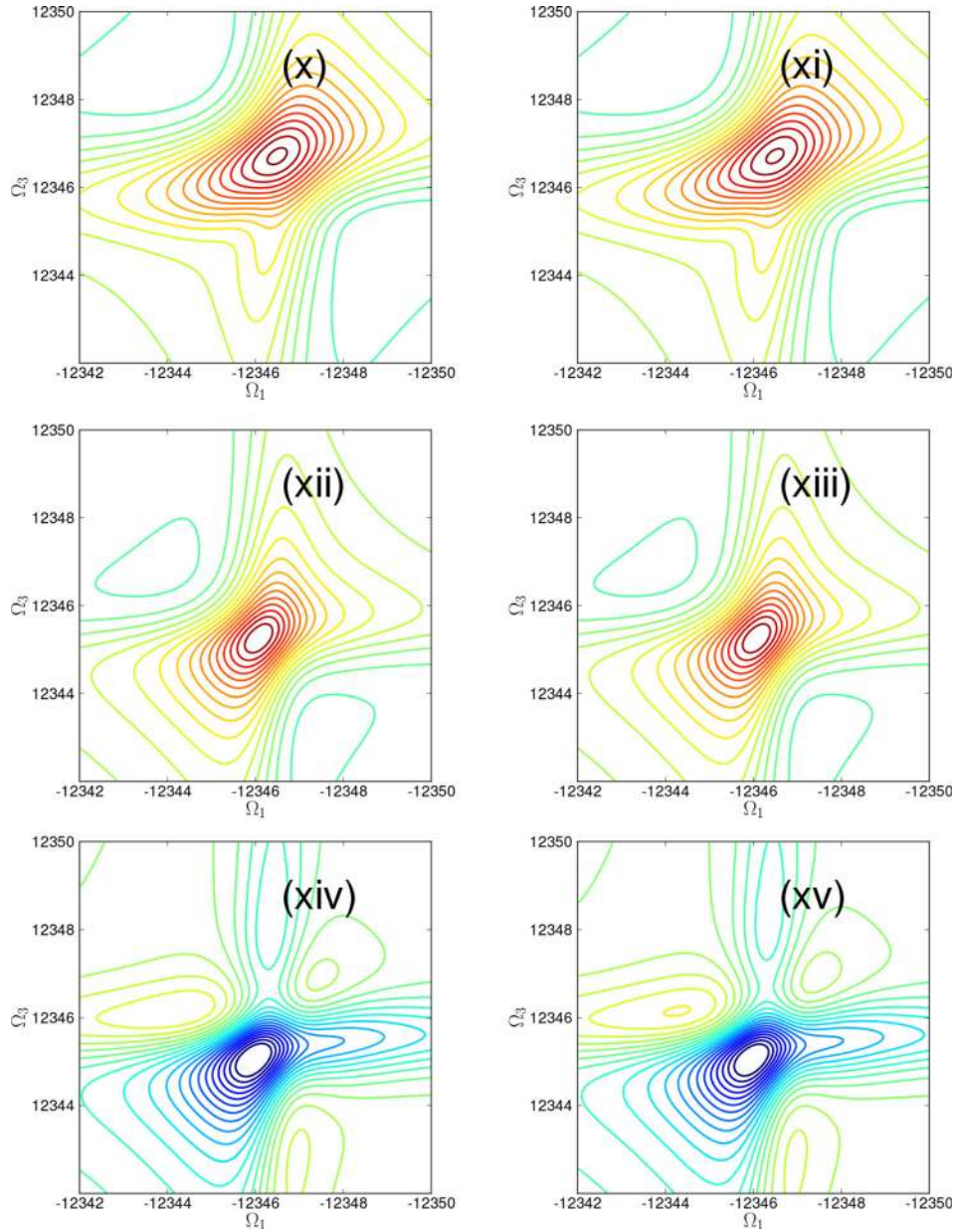
FIG. 12. Contributions from the third block, nonchiral parts of the V_L vector, scaled to $\pm 9 \times 10^{-4}$, $\pm 9 \times 10^{-4}$, $\pm 3 \times 10^{-3}$, $\pm 3 \times 10^{-3}$, $\pm 1 \times 10^{-3}$, $\pm 1 \times 10^{-3}$, respectively.

VI. CONCLUSIONS

The selection rules for the X-ray photon echo signal make the collinear signal independent of intercore distances for both homonuclear and heteronuclear experiments. For homonuclear experiments with variable wave vectors, the spatial phases corresponding to the core positions have to be taken into account. We have simulated the photon echo signal, including a rotationally averaged complex exponential spatial phase corresponding to each core position without recourse to a Taylor expansion in this phase. This formalism was applied to a selenium dipeptide, where the selenium atoms were separated by a convenient distance, in which the nondipole contributions to the signal were expected to be large (see Fig. 9). Similar situations will be encountered frequently in hard X-ray nonlinear spectroscopy of the heavier elements.
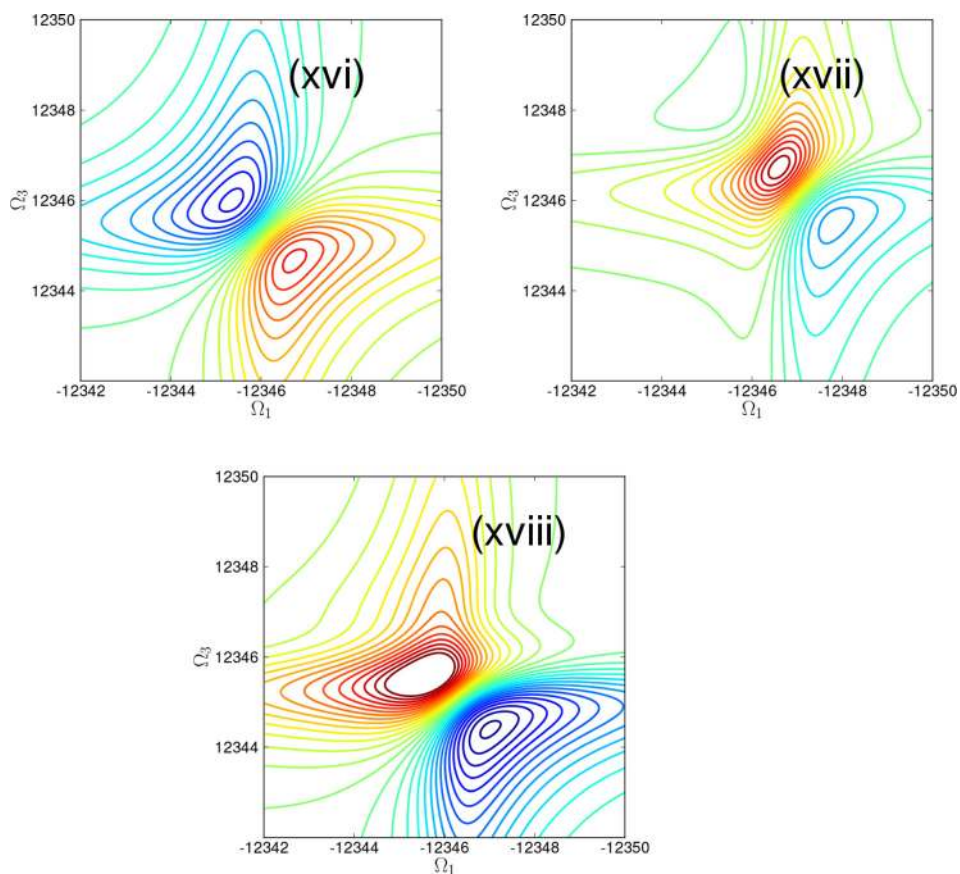
FIG. 13. Contributions from the fourth block, nonchiral parts of the V_L vector, scaled to $\pm 2 \times 10^{-2}$, $\pm 3 \times 10^{-6}$, $\pm 7 \times 10^{-4}$, respectively.

With our choice of pulse bandwidth, and the assumption of four active virtual and occupied orbitals, there are 16 states in the $|g'\rangle$ and $|f_{NM}\rangle$ bands, and 8 states in the singly excited $|e_N, e'_M\rangle$ band, leading to 4096 combinations contributing to the signal. Individual contributions from core-excitations to different virtual orbitals are largely obscured by broadening due to the
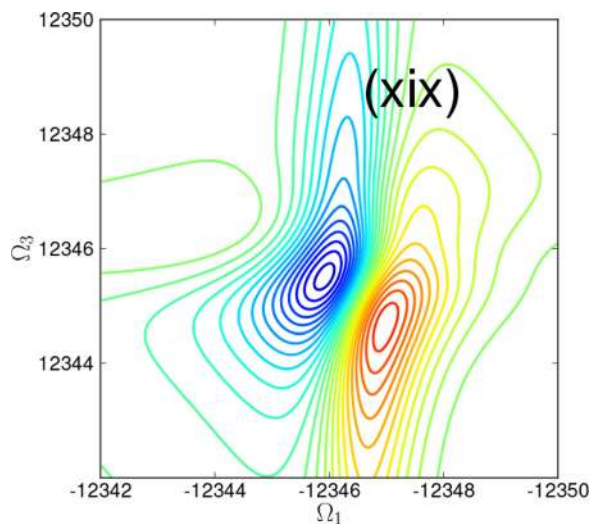

FIG. 14. Contributions from the last and most intense nonchiral matrix element of the V_L vector, scaled to ± 1.
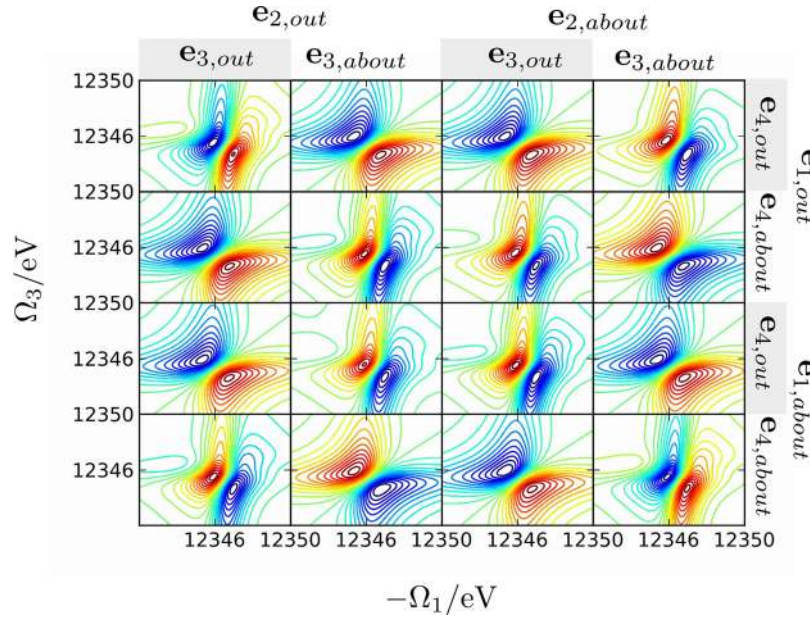
FIG. 15. Polarization dependence of signals with the boxcar geometry. Polarizations are defined in Fig. 7.

short core-hole lifetime at hard x-ray excitation energies. It may be possible to fit the interatomic distance between the cores by simulation, although it would be difficult to imagine a model compound that smoothly interpolates this distance in steps small compared with the X-ray wavelength.

The present results can be extended in various ways. The general excitonic response with collinear pulses should be explored, especially comparing the weak, $S_{XXXY}(\Omega_3, t_2, \Omega_1)$ chiral signal calculated using Taylor expansions to the full analytic treatment described here. Also, for the X-ray experiment, we have noted but not exploited the fact that different diagrams depend on different wave vector differences. By taking the numerical derivative of the signal with respect to the wave vector directions, and holding the other two wave vectors fixed, we could isolate peaks from only one pair of diagrams or the other, as in Ref. 21. This should extend the chiral discrimination of the X-ray signal described here.

ACKNOWLEDGMENTS

APPENDIX A: ROTATIONAL AVERAGING IN NONLINEAR SPECTROSCOPY

In this section, we explain how rotational averaging enters into the expressions for nonlinear spectroscopy. The field of nonlinear spectroscopy is too broad to summarize here, for a more detailed description, we refer the reader to Refs. 4, 5, and 36. In four-wave-mixing spectroscopies such as the photon echo technique, the material interacts with three pulses with wave vectors $\mathbf{k}_{1,\ldots,3}$, resulting in a time-dependent polarization

$$\langle \mu(\mathbf{r}, t) \rangle = \langle \psi(t) | \mu(\mathbf{r}) | \psi(t) \rangle. \tag{A1}$$

The signal is measured in a particular direction ($\mathbf{k}_s = -\mathbf{k}_1 + \mathbf{k}_2 + \mathbf{k}_3$ for the photon-echo signal) and is expressed as a function of the delays between the pulses $t_{1,2,3}$, or their Fourier transforms, with the frequencies $\Omega_{1,2,3}$. We follow the convention in this paper of expressing this signal as a Fourier transform of the first and last interpulse delays, and retaining t_2 as a parameter. The wave function is expanded perturbatively in the applied fields

$$|\psi(t)\rangle = \sum_{n=0}^{3} |\psi^{(n)}(t)\rangle, \tag{A2}$$

$$|\psi^{(n)}(t)\rangle = \left(\frac{-i}{\hbar}\right)^n \int_0^\infty \mathrm{d}\, t_{n-1} \cdots \int_0^\infty \mathrm{d}\, t_1 \hat{\mathcal{H}}_{\mathrm{int}}(t)\hat{\mathcal{H}}_{\mathrm{int}}(t - t_{n-1}) \cdots \hat{\mathcal{H}}_{\mathrm{int}}(t - t_{n-1} - \cdots - t_1), \tag{A3}$$

where the interaction Hamiltonian was defined in Sec. II

$$\hat{\mathcal{H}}_{\mathrm{int}}(t) = -\int \mu(\mathbf{r}, t) \cdot \mathbf{E}(\mathbf{r}, t)\mathrm{d}\,\mathbf{r}. \tag{A4}$$

The field is the sum of four pulses (Eq. (7))

$$E(\mathbf{r}, t) = \sum_{j=1}^{4} \mathbf{e}_j \varepsilon_j(t - \tau_j)\exp[+i\mathbf{k}_j \cdot \mathbf{r} - i\omega_j(t - \tau_j)] + \mathrm{c.c},$$

and the dipole operator defined in Eqs. (10)–(12). Each term in the perturbative expansion of the bra and the ket can be labelled with a Feynman diagram, the rules for selecting only resonant terms are described elsewhere.[4,5,36] The spatial integration in Eq. (A4) means that each interaction with the dipole operator results in a complex exponential factor, $\exp[i\mathbf{k} \cdot \mathbf{R}_N]$. In the dipole approximation $\mathbf{k} \cdot \mathbf{R}_N \ll 1$, and the final signal is written as a linear combination of terms which are proportional to rotationally averaged products of dot products between the molecular dipole operator the pulse polarization vectors

$$S \propto \langle(\boldsymbol{\mu}_1 \cdot \mathbf{e}_1)(\boldsymbol{\mu}_2 \cdot \mathbf{e}_2)(\boldsymbol{\mu}_3 \cdot \mathbf{e}_3)(\boldsymbol{\mu}_4 \cdot \mathbf{e}_4)\rangle, \tag{A5}$$

where the angle brackets denote a rotational average $\langle \cdots \rangle = \int \mathrm{d}\,\hat{l}$. Using the integral form, the term in Eq. (A5) is proportional to

$$\mu_{1;m_1}\mu_{2;m_2}\mu_{3;m_3}\mu_{4;m_4}\langle l_{m_1 f_1} l_{m_2 f_2} l_{m_3 f_3} l_{m_4 f_4}\rangle e_{1;f_1} e_{2;f_2} e_{3;f_3} e_{4;f_4}. \tag{A6}$$

For the local dipole approximation, each dipole moment includes a phase. For the X-ray, stationary core-hole case, the signal is proportional to a product of dot products times a single exponential phase factor

$$S_{\mathrm{non\text{-}dipole}} \propto \langle l_{m_1 f_1} l_{m_2 f_2} l_{m_3 f_3} l_{m_4 f_4}\exp[i\mathbf{k} \cdot \mathbf{R}]\rangle. \tag{A7}$$

Analytic expressions for this rotational average were derived in Ref. 19 and are presented below.

APPENDIX B: ROTATIONALLY AVERAGED SIGNALS

Expressions for the rotational averaging tensor were given in (Eqs. (3.12)–(3.17) in Ref. 19). $\mathbf{R}$ and $\mathbf{k}$ are the distance and wave vector relevant for each peak in the spectrum, R and k are their respective lengths, and $\hat{\mathbf{R}} = \mathbf{R}/R$ and $\hat{\mathbf{k}} = \mathbf{k}/k$ are the unit vectors. $\kappa = Rk = R/\lambda_k$ is the weighting factor that controls which blocks contribute to the signal

$$I_{m_1 m_2 m_3 m_4; f_1 f_2 f_3 f_4}(\mathbf{R}, \mathbf{k}) = \langle l_{m_1 f_1} l_{m_2 f_2} l_{m_3 f_3} l_{m_4 f_4} \exp[i\mathbf{k}_{21} \cdot \mathbf{R}_{nm}] \rangle$$

$$= \mathbf{V}_L^T(\hat{\mathbf{R}}) \mathbf{M}(\kappa) \mathbf{V}_R(\hat{\mathbf{k}}) \tag{B1}$$

$$= \begin{pmatrix} V_{L0} \\ V_{L1} \\ V_{L2} \\ V_{L3} \\ V_{L4} \end{pmatrix}^T \begin{pmatrix} M_0 & 0 & 0 & 0 & 0 \\ 0 & M_1 & 0 & 0 & 0 \\ 0 & 0 & M_2 & 0 & 0 \\ 0 & 0 & 0 & M_3 & 0 \\ 0 & 0 & 0 & 0 & M_4 \end{pmatrix} \begin{pmatrix} V_{R0} \\ V_{R1} \\ V_{R2} \\ V_{R3} \\ V_{R4} \end{pmatrix}. \tag{B2}$$

The first vector is

$$V_0 = \begin{pmatrix} \delta_{\nu_1 \nu_2} \delta_{\nu_3 \nu_4} \\ \delta_{\nu_1 \nu_3} \delta_{\nu_2 \nu_4} \\ \delta_{\nu_1 \nu_4} \delta_{\nu_2 \nu_3} \end{pmatrix}, \tag{B3}$$

where $\nu = m$ when $V_0 = V_{L0}$, and $\nu = f$ when $V_0 = V_{R0}$. The weighting matrix is block diagonal; the first element,

$$M_0 = \frac{j_0(\kappa)}{30} \begin{bmatrix} 4 & -1 & -1 \\ -1 & 4 & -1 \\ -1 & -1 & 4 \end{bmatrix}, \tag{B4}$$

is equivalent to the tensor components contributing to the signal in the dipole approximation. Each block M_n in the matrix $\mathbf{M}$ is weighted by the spherical Bessel function[37]

$$j_n(\kappa) = (-\kappa)^n \left(\frac{1}{\kappa} \frac{d}{d\kappa} \right)^n \frac{\sin(\kappa)}{\kappa}, \tag{B5}$$

where its argument $\kappa = kR = R/\lambda$ is the ratio between the intercore distance and the resonant wavelength. The remaining contributions are written using the same notation

$$V_1(\hat{\mathbf{R}}) = \sum_{\nu_\tau} \begin{pmatrix} \epsilon_{\nu_1 \nu_2 \nu_\tau} \hat{R}_{\nu_\tau} \delta_{\nu_3 \nu_4} \\ \epsilon_{\nu_1 \nu_3 \nu_\tau} \hat{R}_{\nu_\tau} \delta_{\nu_2 \nu_4} \\ \epsilon_{\nu_1 \nu_4 \nu_\tau} \hat{R}_{\nu_\tau} \delta_{\nu_2 \nu_3} \\ \epsilon_{\nu_2 \nu_3 \nu_\tau} \hat{R}_{\nu_\tau} \delta_{\nu_1 \nu_4} \\ \epsilon_{\nu_2 \nu_4 \nu_\tau} \hat{R}_{\nu_\tau} \delta_{\nu_1 \nu_3} \\ \epsilon_{\nu_3 \nu_4 \nu_\tau} \hat{R}_{\nu_\tau} \delta_{\nu_1 \nu_2} \end{pmatrix}, \tag{B6}$$

$$M_1 = \frac{ij_1(\kappa)}{10} \begin{bmatrix} 3 & -1 & -1 & 1 & 1 & 0 \\ -1 & 3 & -1 & -1 & 0 & 1 \\ -1 & -1 & 3 & -0 & -1 & -1 \\ 1 & -1 & 0 & 3 & -1 & 1 \\ 1 & 0 & -1 & -1 & 3 & -1 \\ 0 & 1 & -1 & 1 & -1 & 3 \end{bmatrix}, \tag{B7}$$

$$V_2 = \begin{pmatrix} \delta_{\nu_1\nu_2}\left(\hat{R}_{\nu_3}\hat{R}_{\nu_4} - \frac{1}{3}\delta_{\nu_3\nu_4}\right) \\ \delta_{\nu_1\nu_3}\left(\hat{R}_{\nu_2}\hat{R}_{\nu_4} - \frac{1}{3}\delta_{\nu_2\nu_4}\right) \\ \delta_{\nu_1\nu_4}\left(\hat{R}_{\nu_2}\hat{R}_{\nu_3} - \frac{1}{3}\delta_{\nu_2\nu_3}\right) \\ \delta_{\nu_2\nu_3}\left(\hat{R}_{\nu_1}\hat{R}_{\nu_4} - \frac{1}{3}\delta_{\nu_1\nu_4}\right) \\ \delta_{\nu_2\nu_4}\left(\hat{R}_{\nu_1}\hat{R}_{\nu_3} - \frac{1}{3}\delta_{\nu_1\nu_3}\right) \\ \delta_{\nu_3\nu_4}\left(\hat{R}_{\nu_1}\hat{R}_{\nu_2} - \frac{1}{3}\delta_{\nu_1\nu_2}\right) \end{pmatrix}, \tag{B8}$$

$$M_2 = \frac{-j_2(\kappa)}{14}\begin{bmatrix} 11 & -3 & -3 & -3 & -3 & 4 \\ -3 & 11 & -3 & -3 & 4 & -3 \\ -3 & -3 & 11 & 4 & -3 & -3 \\ -3 & -3 & 4 & 11 & -3 & -3 \\ -3 & 4 & -3 & -3 & 11 & -3 \\ 4 & -3 & -3 & -3 & -3 & 11 \end{bmatrix}, \tag{B9}$$

$$V_3 = \sum_{\nu_\tau} \begin{pmatrix} \varepsilon_{\nu_1\nu_3\nu_\tau}\left[\hat{R}_{\nu_2}\hat{R}_{\nu_4}\hat{R}_{\nu_\tau} - \frac{1}{5}(\delta_{\nu_2\nu_\tau}\hat{R}_{\nu_4} + \delta_{\nu_4\nu_\tau}\hat{R}_{\nu_2} + \delta_{\nu_2\nu_4}\hat{R}_{\nu_\tau})\right] \\ \varepsilon_{\nu_2\nu_3\nu_\tau}\left[\hat{R}_{\nu_1}\hat{R}_{\nu_4}\hat{R}_{\nu_\tau} - \frac{1}{5}(\delta_{\nu_1\nu_\tau}\hat{R}_{\nu_4} + \delta_{\nu_4\nu_\tau}\hat{R}_{\nu_1} + \delta_{\nu_1\nu_4}\hat{R}_{\nu_\tau})\right] \\ \varepsilon_{\nu_3\nu_4\nu_\tau}\left[\hat{R}_{\nu_1}\hat{R}_{\nu_2}\hat{R}_{\nu_\tau} - \frac{1}{5}(\delta_{\nu_1\nu_\tau}\hat{R}_{\nu_2} + \delta_{\nu_2\nu_\tau}\hat{R}_{\nu_1} + \delta_{\nu_1\nu_2}\hat{R}_{\nu_\tau})\right] \end{pmatrix}, \tag{B10}$$

$$M_3 = \frac{-5ij_3(\kappa)}{8}\begin{bmatrix} 3 & -1 & 1 \\ -1 & 3 & 1 \\ 1 & 1 & 3 \end{bmatrix}, \tag{B11}$$

$$V_4 = \left(\hat{R}_{\nu_1}\hat{R}_{\nu_2}\hat{R}_{\nu_3}\hat{R}_{\nu_4} - \frac{1}{7}(\delta_{\nu_1\nu_2}\hat{R}_{\nu_3}\hat{R}_{\nu_4} + \delta_{\nu_1\nu_3}\hat{R}_{\nu_2}\hat{R}_{\nu_4} + \delta_{\nu_1\nu_4}\hat{R}_{\nu_2}\hat{R}_{\nu_3} + \delta_{\nu_2\nu_3}\hat{R}_{\nu_1}\hat{R}_{\nu_4}\right.$$
$$\left. + \delta_{\nu_2\nu_4}\hat{R}_{\nu_1}\hat{R}_{\nu_3} + \delta_{\nu_3\nu_4}\hat{R}_{\nu_1}\hat{R}_{\nu_2}) + \frac{1}{35}(\delta_{\nu_1\nu_2}\delta_{\nu_3\nu_4} + \delta_{\nu_1\nu_3}\delta_{\nu_2\nu_4} + \delta_{\nu_1\nu_4}\delta_{\nu_2\nu_3})\right), \tag{B12}$$

$$M_4 = \frac{35j_4(\kappa)}{8}(1).$$

The full phase averaged isotropic tensor is a vector function of the polarizations $\hat{e}_{1...4}$, the transition dipoles $\hat{\mu}_{1...4}$, and the wave vector Δk and core position $\Delta \mathbf{R}$ differences for each Liouville space pathway.

[1] P. Hamm, M. Lim, and R. M. Hochstrasser, "Structure of the amide i band of peptides measured by femtosecond nonlinear-infrared spectroscopy," J. Phys. Chem. B **102**, 6123–6138 (1998).

[2] S. T. Roberts, K. Ramasesha, and A. Tokmakoff, "Structural rearrangements in water viewed through two-dimensional infrared spectroscopy," Acc. Chem. Res. **42**(9), 1239–1249 (2009).

[3] T. Brixner, J. Stenger, H. M. Vaswani, M. Cho, R. E. Blankenship, and G. R. Fleming, "Two-dimensional spectroscopy of electronic couplings in photosynthesis," Nature **434**, 625–628 (2005).

[4] D. Abramavicius, B. Palmieri, D. V. Voronine, F. Sanda, and S. Mukamel, "Coherent multidimensional optical spectroscopy of excitons in molecular aggregates; quasiparticle versus supermolecule perspectives," Chem. Rev. **109**, 2350–2408 (2009).

[5] S. Mukamel, *Principles of Nonlinear Optical Spectroscopy* (Oxford University Press, USA, 1999).

[6] J. Kim, V. M. Huxter, C. Curutchet, and G. D. Scholes, "Measurement of ElectronElectron interactions and correlations using two-dimensional electronic double-quantum coherence spectroscopy," J. Phys. Chem. A **113**, 12122–12133 (2009).

[7] G. R. Fleming, G. D. Scholes, and Y.-C. Cheng, "Quantum effects in biology," Procedia Chem. **3**(1), 38–57 (2011).

[8] E. Collini and G. D. Scholes, "Coherent intrachain energy migration in a conjugated polymer at room temperature," Science **323**, 369–373 (2009).

[9] J. Murphy and C. Pellegrini, "Introduction to the physics of the free electron laser," in *Frontiers of Particle Beams*, edited by M. Month and S. Turner (Springer-Verlag, Berlin, 1988), Vol. 296, pp. 163–219.

[10] P. H. Bucksbaum, R. Coffee, N. Berrah, P. B. E. Arimondo, and C. Lin, "The first atomic and molecular experiments at the linac coherent light source X-Ray free electron laser," in *Advances in Atomic, Molecular, and Optical Physics* (Academic Press, 2011), Vol. 60, Chap. 5, pp. 239–289.

[11] J. Marangos, "Introduction to the new science with x-ray free electron lasers," Contemp. Phys. **52**, 551–569 (2011).

[12] J. D. Biggs, Y. Zhang, D. Healion, and S. Mukamel, "Two-dimensional stimulated resonance Raman spectroscopy of molecules with broadband x-ray pulses," J. Chem. Phys. **136**, 174117 (2012).

[13] J. D. Biggs, Y. Zhang, D. Healion, and S. Mukamel, "Multidimensional x-ray spectroscopy of valence and core excitations in cysteine," J. Chem. Phys. **138**, 144303 (2013).

[14] D. Healion, J. D. Biggs, and S. Mukamel, "Manipulating one- and two-dimensional stimulated-x-ray resonant-Raman signals in molecules by pulse polarizations," Phys. Rev. A **86**, 033429 (2012).

[15] Y. Zhang, J. D. Biggs, D. Healion, N. Govind, and S. Mukamel, "Core and valence excitations in resonant x-ray spectroscopy using restricted excitation window time-dependent density functional theory," J. Chem. Phys. **137**, 194306 (2012).

[16] A. Salam, *Molecular Quantum Electrodynamics: Theory of Long-Range Intermolecular Interactions* (Wiley, Hoboken, NJ, 2010).

[17] D. L. Andrews and T. Thirunamachandran, "On three-dimensional rotational averages," J. Chem. Phys. **67**, 5026–5033 (1977).

[18] D. Abramavicius and S. Mukamel, "Coherent third-order spectroscopic probes of molecular chirality," J. Chem. Phys. **122**, 134305 (2005).

[19] D. L. Andrews and M. J. Harlow, "Phased and Boltzmann-weighted rotational averages," Phys. Rev. A **29**(5), 2796 (1984).

[20] I. P. Mercer, Y. C. El-Taha, N. Kajumba, J. P. Marangos, J. W. G. Tisch, M. Gabrielsen, R. J. Cogdell, E. Springate, and E. Turcu, "Instantaneous mapping of coherently coupled electronic transitions and energy transfers in a photosynthetic complex using angle-resolved coherent optical wave-mixing," Phys. Rev. Lett. **102**, 057402 (2009).

[21] I. P. Mercer, "Angle-resolved coherent optical wave mixing," Phys. Rev. A **82**, 043406 (2010).

[22] I. Schweigert and S. Mukamel, "Double-quantum-coherence attosecond X-ray spectroscopy of spatially separated, spectrally overlapping core-electron transitions," Phys. Rev. A **78**, 052509 (2008).

[23] R. R. Ernst, G. Bodenhausen, and A. Wokaun, *Principles of Nuclear Magnetic Resonance in One and Two Dimensions* (Oxford University Press, USA, 1990).

[24] Z. Zhang, K. L. Wells, M. T. Seidel, and H.-S. Tan, "Fifth-order three-dimensional electronic spectroscopy using a Pump-Probe configuration," J. Phys. Chem. B (published online).

[25] Z. Zhang, K. L. Wells, and H.-S. Tan, "Purely absorptive fifth-order three-dimensional electronic spectroscopy," Opt. Lett. **37**, 5058–5060 (2012).

[26] Z. Zhang, K. L. Wells, E. W. J. Hyland, and H.-S. Tan, "Phase-cycling schemes for pumpprobe beam geometry two-dimensional electronic spectroscopy," Chem. Phys. Lett. **550**, 156–161 (2012).

[27] H.-S. Tan, "Theory and phase-cycling scheme selection principles of collinear phase coherent multi-dimensional optical spectroscopy," J. Chem. Phys. **129**, 124501 (2008).

[28] W. A. Hendrickson, "Synchrotron crystallography," Trends Biochem. Sci. **25**, 637–643 (2000).

[29] M. Teplova, C. J. Wilds, Z. Wawrzak, V. Tereshko, Q. Du, N. Carrasco, Z. Huang, and M. Egli, "Covalent incorporation of selenium into oligonucleotides for x-ray crystal structure determination via MAD: proof of principle," Biochimie **84**, 849–858 (2002).

[30] T. M. Vishwanatha, N. Narendra, B. Chattopadhyay, M. Mukherjee, and V. V. Sureshbabu, "Synthesis of selenoxo peptides and oligoselenoxo peptides employing LiAlHSeH," J. Org. Chem. **77**, 2689–2702 (2012).

[31] M. J. Frisch, G. W. Trucks, H. B. Schlegel, G. E. Scuseria, M. A. Robb, J. R. Cheeseman, J. A. Montgomery, Jr., T. Vreven, K. N. Kudin, J. C. Burant, J. M. Millam, S. S. Iyengar, J. Tomasi, V. Barone, B. Mennucci, M. Cossi, G. Scalmani, N. Rega, G. A. Petersson, H. Nakatsuji, M. Hada, M. Ehara, K. Toyota, R. Fukuda, J. Hasegawa, M. Ishida, T. Nakajima, Y. Honda, O. Kitao, H. Nakai, M. Klene, X. Li, J. E. Knox, H. P. Hratchian, J. B. Cross, V. Bakken, C. Adamo, J. Jaramillo, R. Gomperts, R. E. Stratmann, O. Yazyev, A. J. Austin, R. Cammi, C. Pomelli, J. W. Ochterski, P. Y. Ayala, K. Morokuma, G. A. Voth, P. Salvador, J. J. Dannenberg, V. G. Zakrzewski, S. Dapprich, A. D. Daniels, M. C. Strain, O. Farkas, D. K. Malick, A. D. Rabuck, K. Raghavachari, J. B. Foresman, J. V. Ortiz, Q. Cui, A. G. Baboul, S. Clifford, J. Cioslowski, B. B. Stefanov, G. Liu, A. Liashenko, P. Piskorz, I. Komaromi, R. L. Martin, D. J. Fox, T. Keith, M. A. Al-Laham, C. Y. Peng, A. Nanayakkara, M. Challacombe, P. M. W. Gill, B. Johnson, W. Chen, M. W. Wong, C. Gonzalez, and J. A. Pople, GAUSSIAN 09, Gaussian Inc. Wallingford, CT, 2009.

[32] P. J. Stephens, F. J. Devlin, C. F. Chabalowski, and M. J. Frisch, "Ab initio calculation of vibrational absorption and circular dichroism spectra using density functional force fields," J. Phys. Chem. **98**, 11623–11627 (1994).

[33] R. A. Kendall, T. H. Dunning, and R. J. Harrison, "Electron affinities of the first row atoms revisited. Systematic basis sets and wave functions," J. Chem. Phys. **96**, 6796–6806 (1992).

[34] D. E. Woon and T. H. Dunning, "Gaussian basis sets for use in correlated molecular calculations. III. The atoms aluminum through argon," J. Chem. Phys. **98**, 1358–1371 (1993).

[35] G. H. Zschornack, *Handbook of X-Ray Data*, 1 ed. (Springer, 2007).

[36] S. Mukamel and D. Abramavicius, "Many-body approaches for simulating coherent nonlinear spectroscopies of electronic and vibrational excitons," Chem. Rev. **104**, 2073–2098 (2004).

[37] M. Abramowitz and I. Stegun, *Handbook of Mathematical Functions* (Dover, New York, 1964).